Physics of Fluids

Comments on the numerical investigation of Rayleigh and Marangoni convection in a vertical circular cylinder

Cite as: Physics of Fluids **6**, 1425 (1994); https://doi.org/10.1063/1.868257
Submitted: 17 November 1992 • Accepted: 03 December 1993 • Published Online: 02 September 1998

Claus Wagner, Rainer Friedrich and Ranga Narayanan


View Online

Export Citation

ARTICLES YOU MAY BE INTERESTED IN

On the onset of convective instabilities in cylindrical cavities heated from below. I. Pure thermal case
Physics of Fluids **11**, 2078 (1999); https://doi.org/10.1063/1.870070

Solute induced jittery motion of self-propelled droplets
Physics of Fluids **33**, 022103 (2021); https://doi.org/10.1063/5.0038716

Oscillatory Marangoni convection in cylindrical liquid bridges
Physics of Fluids **8**, 2906 (1996); https://doi.org/10.1063/1.869070

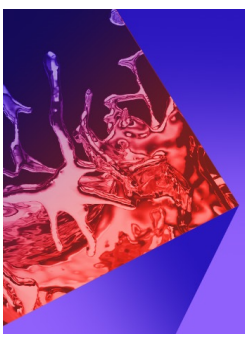
Physics of Fluids
Special Topic: Paint and Coating Physics
Submit Today!

AIP Publishing

© 1994 American Institute of Physics.

Comments on the numerical investigation of Rayleigh and Marangoni convection in a vertical circular cylinder

Claus Wagner and Rainer Friedrich
Lehrstuhl für Fluidmechanik, T. U. München, Arcisstrasse 21, D8000 München 40, Germany

Ranga Narayanan
Department of Chemical Engineering, University of Florida, Gainesville, Florida 32611

(Received 17 November 1992; accepted 3 December 1993)

Convection in a cylindrical container was simulated with a three-dimensional, time-dependent code. For the case of purely Rayleigh convection, a completely rigid cylinder with adiabatic vertical walls and conducting horizontal walls was considered. The calculations showed that the individual velocity components could be in a transient state, while the total heat transfer was steady. This occurred in cases where the maximum azimuthal component of velocity was very small in magnitude, in comparison to the other two components, and this component decreased in time. On the other hand, the total kinetic energy along with the heat transfer reached a steady value. Consequently the present results have been shown to be at variance with the calculations of Neumann [J. Fluid Mech. **214**, 559 (1990)]. Marangoni convection was modeled with a free flat surface on the upper side, assuming the superimposed second layer to be passive. The numerically obtained critical Marangoni numbers and flow patterns were compared favorably to earlier results from linearized stability. In addition, flow structural changes for supercritical Marangoni numbers were illustrated. Interestingly, axisymmetric disturbances led to nonsymmetric bifurcation diagrams, but three-dimensional disturbance calculations led to symmetry in the bifurcation plots. Another very interesting result was the observed transition from three-dimensional to two-dimensional patterns as the Marangoni number was increased. Large computational requirements precluded a detailed parametric study. The special case of Prandtl number equal to 6.7 (corresponding to water), and in the case of Marangoni convection, a surface Biot number of unity was assumed.

I. BRIEF BACKGROUND

We now divide the background work into two cases, viz., (a) the upper rigid wall or pure Rayleigh problem and upper free surface or pure Marangoni problem.

A. Rigid upper surface case

Experimentalists have found that the cellular structure expected is affected by the shape of the bounding sidewalls. In particular, work by Koschmieder[1] and Stork and Müller[2] indicates the strong influence on planform structure by the geometry of the container. The existence of the nonaxisymmetric flow state for larger aspect ratios in right circular geometries was established experimentally in several studies. Noteworthy are those of Ostromunov *et al.*[3] and Müller *et al.*[4] The latter reported observing the axisymmetric flow state at $\beta=1.0$ (here β is the aspect ratio and is given by the ratio of height of the liquid layer to its radius) and a nonaxisymmetric pattern at $\beta\geqslant 2.0$ for both water (Prandtl number or $\mathrm{Pr}=6.7$) and liquid gallium ($\mathrm{Pr}=0.02$).

Charlson and Sani[5] calculated a transition in the initial dynamic state from an axisymmetric to a nonaxisymmetric flow as the aspect ratio was increased above $\beta=1.23$ for insulating sidewalls and $\beta=1.64$ for conducting sidewalls. In a recent paper, Hardin *et al.*[6] corrected some of the results of Charlson and Sani[5] and extended them for linearized thermosolutal convection with a Soret effect.

There have been some more three-dimensional numerical studies on buoyancy-driven convection in vertical cylinders, mainly by Crespo *et al.*[7] and Neumann.[8] This work was concerned with nonlinear convection, i.e., convection in the post-onset region. The work of the latter covered steady and oscillatory, as well as two- and three-dimensional buoyancy-driven flow in a cylinder. Neumann calculated the velocity and the temperature distributions in a vertical circular cylinder for various Rayleigh numbers and Prandtl numbers and found that both two- and three-dimensional flow fields could be obtained (depending on the initial temperature disturbance), for the aspect ratio $\beta=1.0$ and $\mathrm{Ra}=2800$. (Neumann defines the aspect ratio as height divided by diameter.) The two-dimensional flow patterns were qualitatively verified by experiments done by Müller *et al.*[4] and Neumann.[9]

B. Free upper surface case

Critical Marangoni numbers were reported by Vrentas *et al.*[10] for a cylinder, where the liquid was superimposed by a passive gas. This was an analytical study and assumed only axisymmetric flows. This study also included a weak nonlinear analysis, which showed the branching behavior with respect to aspect ratio and surface Biot number. It was seen that the transcritical region in the vicinity of the bifurcation from the conductive solution decreased as the radius of the container increased. In this sense the results approached the two-dimensional results of infinite layer theory of Cloot and Lebon.[11] A subsequent study by Win-

 1070-6631/94/6(4)/1425/9/$6.00 © 1994 American Institute of Physics

ters *et al.*[12] for two-dimensional convection in a rectangle also confirmed such qualitative features. The study by Vrentas *et al.*[10] was based on an eigenfunction expansion method.

A study of nonlinear Marangoni convection in a circular cylindrical geometry by Rosenblat *et al.*[13] was performed for the case of vorticity free vertical sidewalls. A refinement of their work was done by Chen *et al.*,[14] where three-dimensional results were given, albeit for a linear case. This latter work assumed the case of physically realistic, rigid, vertical sidewalls and used a Galerkin method in the radial direction and finite differencing in the vertical coordinate.

One purpose of the present work is to determine these critical values numerically by tracing the branches, and compare it to the ones obtained by linearized stability. A second purpose is to depict the velocity and temperature profiles and comment on the nature of the branching from the conductive state. Finally, we are interested in seeing how the transition takes place from three-dimensional to two-dimensional flow structures.

II. GOVERNING EQUATIONS

Our model is concerned with a Newtonian fluid enclosed in a cylindrical container of height H and radius R. The continuity, Navier–Stokes, and energy equation are cast into cylindrical coordinates, where the origin of the coordinate system coincides with the center of the lower boundary. The Boussinesq approximation is invoked. The sidewalls of the cylinder are taken to be perfectly insulated and rigid and the lower boundary is a rigid wall with an isothermal temperature T_1. For the pure Rayleigh case the upper boundary is an isothermal rigid wall with a temperature $T_2<T_1$, but for the Marangoni case the upper boundary is a free surface, superimposed by a passive gas of mean temperature T_2. Introducing the scale factors H for the length, κ/H for velocity, $(\rho\kappa^2)/H^2$ for pressure, H^2/κ for time, and (T_1-T_2) for temperature, where ρ denotes the density and κ the thermal diffusivity, we obtain the following equations in dimensionless form. These are the continuity, momentum, and energy equations, respectively,

$$\nabla\cdot\mathbf{U}=0, \tag{1}$$

$$\frac{\partial\mathbf{U}}{\partial t}=-\nabla p-(\mathbf{U}\cdot\nabla)\mathbf{U}+\mathrm{Pr}\,\nabla^2\mathbf{U}+\mathrm{Ra}\,\mathrm{Pr}\,T\mathbf{e}, \tag{2}$$

$$\frac{\partial T}{\partial t}=-\mathbf{U}\cdot\nabla T+\nabla^2 T. \tag{3}$$

$\mathbf{U}=(U_r,U_\varphi,U_z)$ are the dimensionless velocity components in the cylindrical (r,φ,z) system of coordinates, p and T are the dimensionless pressure and the temperature, respectively, and $\mathbf{e}=(0,0,1)$ is a unit vector in the direction of gravity.

The pertinent dimensionless numbers are defined as follows:

$$\mathrm{Ra}=\frac{\alpha g H^3(T_1-T_2)}{\nu\kappa},\quad \mathrm{Pr}=\frac{\nu}{\kappa}, \tag{4a}$$

$$\mathrm{Ma}=\frac{(\partial\sigma/\partial T)|_{T_0}(T_1-T_2)H}{\mu\kappa},\quad \mathrm{Bi}=\frac{hH}{k},\quad \beta=\frac{H}{R}, \tag{4b}$$

where $\alpha=-(1/\rho_0)(\partial\rho/\partial T|_{T_0})$ is the thermal expansion coefficient, g is the gravitational acceleration, μ is the dynamic viscosity, ν is the kinematic viscosity, h is the heat transfer coefficient, and k is the thermal conductivity. The subscript "0" indicates evaluation at a reference point.

For the buoyancy-driven convection we consider all walls to be rigid, leading to the no-slip velocity boundary conditions. For the case of surface tension-driven convection we assume the following conditions of radial and azimuthal stress at the upper surface:

$$\frac{\partial U_r}{\partial z}+\frac{\partial U_z}{\partial r}+\mathrm{Ma}\frac{\partial T}{\partial r}=0, \tag{5}$$

$$\frac{\partial U_\varphi}{\partial z}+\frac{\partial U_z}{r\,\partial\varphi}+\mathrm{Ma}\frac{\partial T}{r\,\partial\varphi}=0. \tag{6}$$

The thermal conditions are insulated vertical sidewalls, i.e., the normal temperature gradient vanishes along the vertical walls, isothermal lower and upper walls, and therefore $T_1=0.5$ and $T_2=-0.5$ for the buoyancy case, and in the Marangoni case $T_1=0.5$ and $\partial T/\partial z=\mathrm{Bi}(T+0.5)$, respectively.

The initial conditions are a conductive state with no flow, a linear temperature field $T=0.5-z$, and a temperature balancing pressure field.

III. NUMERICAL METHOD

A finite volume technique is used to solve Eqs. (1)–(3) numerically. It consists of integrating these equations over the cell volume $\Delta V=r\,\Delta r\,\Delta\varphi\,\Delta z$ of an equidistant cylindrical grid. By defining cell surface-averaged velocity components, $(\bar{u}_r,\bar{u}_\varphi,\bar{u}_z)$, the continuity equation is satisfied exactly. These components are determined from the averaged momentum equation via staggered grids. That is, they are determined at faces that are displaced by $\Delta r/2$, $\Delta\varphi/2$, $\Delta z/2$ in the positive (r,φ,z) direction, respectively. Pressure and temperature are defined as cell volume averages and are stored in the cell center. Deviations from these averaged flow quantities within the cell are generally small in laminar flows and do not therefore create noticeable momentum and energy fluxes across the surface. Thus, a set of ordinary differential equations in time is obtained with central finite differences in space:

$$\sum_j \Delta A_j\bar{u}_j|_{(\xi_j+\Delta\xi_j/2)}-\Delta A_j\bar{u}_j|_{[\xi_j-(\Delta\xi_j/2)]}=0, \tag{7}$$

$$\Delta V_i\frac{\partial\bar{u}_i}{\partial t}+\sum_j\left[\Delta A_j(\bar{u}_i\bar{u}_j+\bar{p}\delta_{ij}-\bar{\tau}_{ij})|_{[\xi_j+(\Delta\xi_j/2)]}-\Delta A_j(\bar{u}_i\bar{u}_j+\bar{p}\delta_{ij})-\bar{\tau}_{ij}|_{[\xi_j-(\Delta\xi_j/2)]}\right]-(CT)_i-\mathrm{Ra}\cdot\mathrm{Pr}\cdot\Delta V\bar{T}e_i=0, \tag{8}$$

$$(\Delta V)\frac{\partial \bar{T}}{\partial t}+\sum_j [\Delta A_j(\bar{u}_j\bar{T}-\bar{q}_j)|_{[\xi_j+(\Delta\xi_j/2)]}$$

$$-\Delta A_j(\bar{u}_j\bar{T}-q_j)|_{(\xi_j-\Delta\xi_j/2)}]=0. \tag{9}$$

In these equations, summation over j stands for a summation over the (r,φ,z) directions. Summation convention has not been applied to the above equations and $i=(1,2,3)$ represents the (r,φ,z) coordinates, respectively. The cell surfaces ΔA_j perpendicular to these directions have the values

$$\Delta A_r=r\,\Delta\varphi\,\Delta z,\quad \Delta A_\varphi=\Delta r\,\Delta z,\quad \Delta A_z=r\,\Delta\varphi\,\Delta r.$$

Here ΔV_i stands for the volume of a staggered grid and $\xi_j\pm\Delta\xi_j/2$ for the position of a face perpendicular to the j direction of the corresponding staggered cell. The surface-averaged shear stresses and heat fluxes are defined in the following way:

$$\bar{\tau}_{ij}=\mathrm{Pr}\,\bar{D}_{ij},\quad \bar{q}_j=-\delta_j T. \tag{10}$$

The averaged deformation tensor $\bar{D}_{ij}$ is determined from the averaged velocities, viz.,

$$\bar{D}_{ij}=\begin{vmatrix} 2\delta_r\bar{u}_r & r\delta_r\left(\frac{\bar{u}_\varphi}{r}\right)+\frac{1}{r}\delta_\varphi\bar{u}_r & \delta_z\bar{u}_r+\delta_r\bar{u}_z \\ r\delta_r\left(\frac{\bar{u}_\varphi}{r}\right)+\frac{1}{r}\delta_j\bar{u}_r & \frac{2}{r}(\delta_\varphi u_\varphi+\bar{u}_r) & \frac{1}{r}\delta_\varphi\bar{u}_z+\delta_z\bar{u}_\varphi \\ \delta_z\bar{u}_r+\delta_r\bar{u}_z & \frac{1}{r}\delta_\varphi\bar{u}_z+\delta_z\bar{u}_\varphi & 2\delta_z\bar{u}_z \end{vmatrix}; \tag{11}$$

δ_j is a central finite difference operator and e_i are the components of the unit vector parallel to the gravity vector. Here $(CT)_i$ abbreviates the curvature terms. They read as follows:

$$(CT)_r=\frac{\Delta V}{r}(\bar{u}_\varphi^2-\bar{\tau}_{\varphi\varphi}),$$

$$(CT)_\varphi=\frac{\Delta V}{r}(-\bar{u}_\varphi\bar{u}_r+\bar{\tau}_{\varphi r}), \tag{12}$$

$$(CT)_z=0,$$

and are treated as volume averages. In order to satisfy the incompressibility constraint, we use a method of Chorin.[15] We rewrite (8) and (9) in a symbolic fashion for a discussion of the time integration scheme, viz.,

$$\Delta V\frac{\partial \mathbf{u}}{\partial t}=\mathbf{C}-\Delta p+(\mathbf{CT})+\mathbf{D}+\mathbf{B}, \tag{13}$$

$$\Delta V\frac{\partial T}{\partial t}=C(T)+D(T), \tag{14}$$

C, **CT**, **D**, **B** stand for the convection, curvature, diffusion, and buoyancy terms, whereas $C(T)$ and $D(T)$ denote the convection and diffusion terms in the heat transport equation. Each time step is split into two substeps. In the first, an approximate velocity field $\mathbf{u}^*$ is computed at time $(n+1)$, neglecting the pressure gradient, viz.,

$$\mathbf{u}^*-\frac{1}{2}f_3\frac{\Delta t}{\Delta V}\mathbf{D}_\varphi^{n+1}$$

$$=f_1\mathbf{u}^{n-1}+f_2\mathbf{u}^n+f_3\frac{\Delta t}{\Delta V}[\mathbf{C}^n+(\mathbf{CT})^n+\mathbf{B}^n \tag{15}$$

$$+\mathbf{D}_z^{n-1}+\mathbf{D}_r^{n-1}+\tfrac{1}{2}\mathbf{D}_\varphi^{n-1}].$$

In the second substep, the pressure is computed from a Poisson equation of the form

$$\nabla\cdot\mathbf{u}^*-f_3\frac{\Delta t}{\Delta V}\nabla^2 p=0, \tag{16}$$

which results from taking the divergence of the correction equation

$$\mathbf{u}^{n+1}=\mathbf{u}^*-f_3\frac{\Delta t}{\Delta V}\nabla p, \tag{17}$$

and the continuity equation

$$\nabla\cdot\mathbf{u}^{n+1}=0, \tag{18}$$

is used to update the velocity field. The temperature field is now obtained from

$$T^{n+1}-\frac{1}{2}f_3\frac{\Delta t}{\Delta V}D(T)_\varphi^{n+1}$$

$$=f_1T^{n-1}+f_2T^n+f_3\frac{\Delta t}{\Delta V}[C(T)^n \tag{19}$$

$$+D(T)_{z,r}^{n-1}+\tfrac{1}{2}D(T)_\varphi^{n-1}].$$

The next time step can then be obtained. Here $f_i=(f_1,f_2,f_3)=(1,0,2)$, except for the first step, which is, of course, a Euler step: $f_0=(0,0,1)$. The Poisson equation (16) is solved directly using fast elliptic solvers. A remark may be in order with respect to the singularity of the partial differential equations at the cylinder axis. In the present finite volume formulation, fluxes of mass, momentum, and energy are needed. These vanish for vanishing grid surfaces. Further details on the numerical procedure are given by Schmitt.[16]

In all the simulations, we start with zero velocity components and a linear temperature profile in the axial direction of $T=0.5-z$. Since these data correspond to the state of heat conduction and mechanical equilibrium, we have to impose an initial temperature disturbance in order to start the convection process.

Besides the ordinary boundary conditions for no-mass transfer, no-slip, constant temperature and/or insulation at the rigid walls, the free upper surface requires special treatment. It remains flat, which means the axial velocity component vanishes, and it relates surface tension forces to viscous forces, and this drives the flow. Newton's law of cooling is applied at the free surface. In the cause of brevity the discrete forms of these boundary conditions are not presented here.

In what follows we shall discuss the effect of imposing axisymmetric disturbances as well as three-dimensional disturbances. It may be noted that the code is symmetry preserving, in the sense that an axisymmetric disturbance

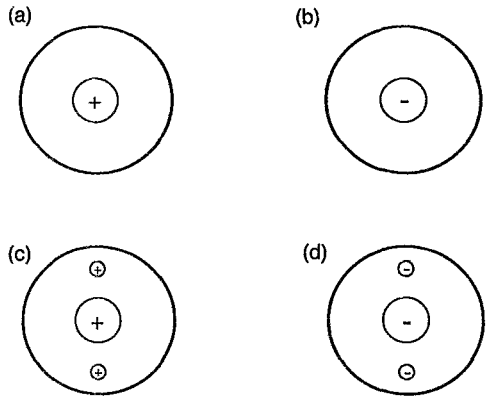

FIG. 1. Left to right (a) positive symmetric, (b) negative symmetric, (c) positive asymmetric, and (d) negative asymmetric temperature disturbance.

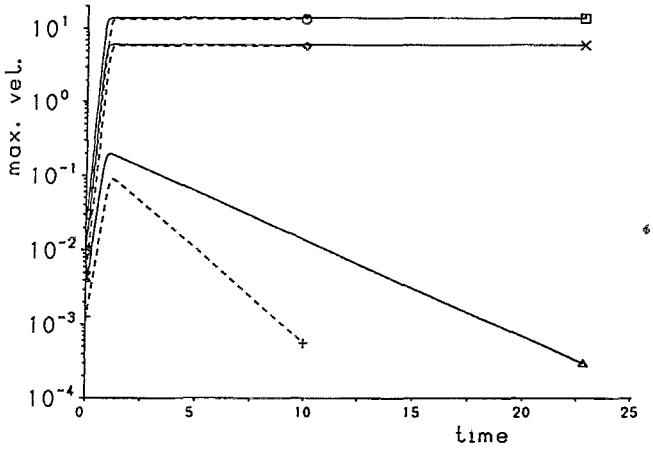

FIG. 2. Maximal velocities over dimensionless time for $\beta=1.0$ and Ra $=2800$, grid for solid lines is $24\times16\times24$, grid for dashed lines is $32\times32\times32$. □ and ○, $U_{z,\max}$; Δ and +, $U_{\varphi,\max}$; × and ◇, $U_{r,\max}$.

will not lead to a three-dimensional steady flow field, since the azimuthal component of velocity will never change from its initial value of zero. On the other hand, a three-dimensional disturbance can ultimately grow into either a two- or three-dimensional flow field, and this will depend on the stability of the different modes.

IV. RESULTS AND CONCLUSIONS OF THE NUMERICAL SIMULATIONS

A. Rayleigh convection with rigid, conducting upper surface (two- and three-dimensional disturbances)

As we were interested in testing our numerical scheme, we redid the calculations of Neumann.[8] In the same manner as Neumann, four different temperature disturbances ($T'<0.01$), as shown in Fig. 1, were applied at the first time step at the position $z=0.5$, and for a Prandtl number of 6.7. The resulting flow field (not shown) was a single axisymmetric toroid with upflow in the center of the cylinder for the positive axisymmetric temperature disturbance and downflow for the negative axisymmetric temperature disturbance. This was in qualitative agreement with the results of Neumann. When we compared the maximum axial velocity, we found a quantitative difference between the maximum absolute value of the vertical component of velocity ($U_{z,\max}$). He got $U_{z,\max}=10.7$ while we obtained $U_{z,\max}=13.82$ for the positive initial disturbance. This could be a result of the different numerical schemes and grid spacing in time and space. In fact, we shall show next that the grid spacing has a definite impact when three-dimensional disturbances are imposed.

For the nonaxisymmetric disturbance shown in Fig. 1(c), Neumann reported a nonaxisymmetric two-roll solution, which he denoted with the mode $m=2$ (here m is the azimuthal wave number[13]). This was obtained for a value of $\beta=1.0$, a conducting rigid upper surface, a Prandtl number of 6.7, and with a Rayleigh number of 2800. We used the same boundary conditions as he did but with different grid sizes, and concluded that a finer grid spacing results in the vanishing of the azimuthal component of velocity. Figure 2 gives the time variation of vertical, azimuthal, and radial components of velocity for various grid sizes. We conclude that a finer mesh will accelerate the decrease of the azimuthal component of velocity to zero. The isotaches of the axial velocity in a cut plane for $z=0.5$ is presented in Fig. 3. The flow is symmetric with an upflow at the axis of the cylinder. For a negative asymmetric temperature disturbance, we obtained a toroid of mode $m=0$, but with downflow on the axis. These flow fields agreed with the ones that both Neumann, and we obtained for symmetric positive and negative disturbances. For simulations with a coarser mesh of $16\times16\times16$ points, the resulting flow field represented a cell of mode $m=2$ similar to the one Neumann reported. In other words, we believe that Neumann's result on three-dimensional flow for this case was an artifact of his coarse mesh size. In fact, the experimental results of Stroebel[17]

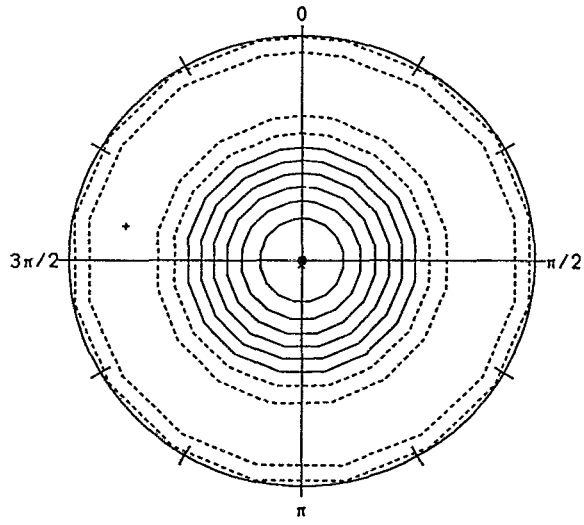

FIG. 3. Isotaches of the axial velocity U_z for $z=0.5$, $24\times16\times24$ grid points; $\beta=1.0$ and Ra$=2800$, Fig. 1(c) disturbance, increment: 0.5506, solid lines $U_z>0$, and dashed lines $U_z<0$.

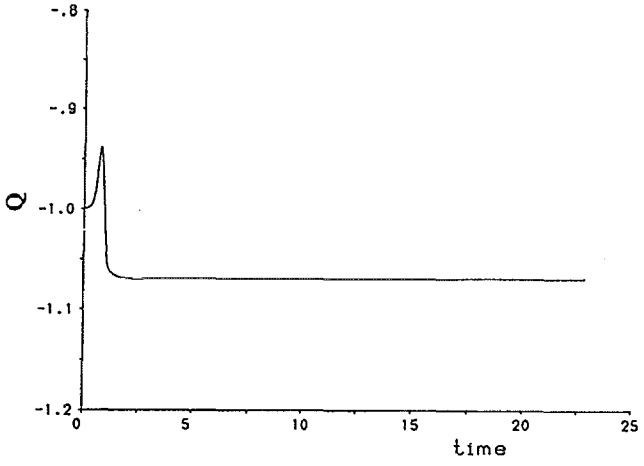

FIG. 4. Heat flux represented by "Q" vs dimensionless time at $z=0$, $24\times16\times24$ grid points, $\beta=1.0$, and Ra=2800.

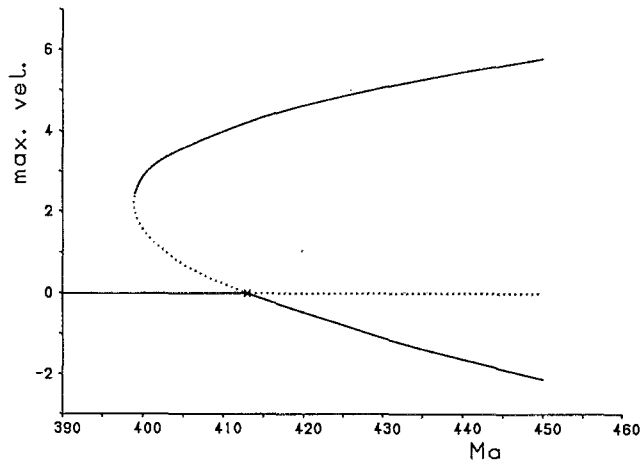

FIG. 5. Bifurcation for Bi=1.0 and $\beta=1.0$, maximal radial velocity $U_{r,\max}$ plotted against Marangoni number. Solid lines: steady flow; dashed line: unstable regime. The bifurcation point is indicated by "x."

indicate a two-dimensional axisymmetric flow for this case. We have used the meshes of $24\times16\times24$ and $32\times32\times32$ points in the (r,φ,z) directions and a time step of $\Delta t=2\times10^{-5}$. We do, however, believe that three-dimensional flow can arise at a different and higher Rayleigh number.

In order to decide whether the flow reached a steady-state Neumann looked at the heat flux across the bottom boundary, $z=0$. To obtain similar information we calculated the sum of the temperature gradients of all grid points and called this "Q." The time evolution of this quantity for the case Ra=2800, Pr=6.7 and for a three-dimensional disturbance is shown in Fig. 4. At about $t=1$, Q or the heat flux into the system seemed to reach a steady state, while the flow was still in a three-dimensional transient state; see Fig. 2. We therefore conclude that if we want to have a sensitive criteria for a steady state of a three-dimensional flow it is important to study the behavior of the velocity components. Even if the total amount of energy going into the system is constant, there are still three degrees of freedom through which the energy can be distributed. In fact, we observed that the total kinetic energy reached a steady value when Q reached a steady value. However, the individual components were still in a transient state. Admittedly, the azimuthal component of velocity was very small compared to the dominant radial and vertical component of velocities. It is therefore likely that Neumann considered his three-dimensional cell of mode $m=2$ as a steady-state solution, while he was actually in a transient state with decreasing azimuthal velocity.

B. Marangoni convection (axisymmetric disturbances)

In this section we give a summary of the calculations for supercritical convection, where axisymmetric disturbances are imposed. We were first interested in obtaining the critical Marangoni number for the case of $\beta=1.0$ for an axisymmetric disturbance, as shown in Fig. 1(a). The value of the critical Marangoni number is independent of the Prandtl number. However, the way in which it is approached as the branches are traced does indeed depend on the value of the Prandtl number. As such, we restricted our calculations throughout to the case of Pr=6.7. We have noted earlier that this corresponds to the case of convection of water. Because of the considerable computation time involved (for a steady flow solution near the bifurcation point about 50 cpu hours on a Cray-YMP were used), we sacrificed generality and restricted the Biot number to be 1. The value of critical Marangoni number is known to depend on this quantity. [We note that the literature often defines the Marangoni number using the temperature difference between the lower plate and the upper surface. The temperature difference in this study is taken to be between the lower plate and the mean temperature in the upper gas phase. As such, the following relationship holds between the Marangoni number used in this study and others such as Chen *et al.*, $(\mathrm{Ma})_{\mathrm{ours}}=(\mathrm{Ma})_{\mathrm{Chen\ et\ al.}}(1+\mathrm{Bi})/\mathrm{Bi}$.] Now the Marangoni number was initially imposed to be Ma $=450$. Calculations were performed and the velocities were obtained. The Marangoni number was then decreased in steps until the velocity components converged to zero. Thus, the bifurcation point from the conductive state was found to occur at Ma=414. Vrentas *et al.*[10] gave a critical value of Ma=412 for $\beta=1.0$ and a Biot number of unity. For each value of the Marangoni number, a steady state was achieved, and the maximal radial velocity plotted over Ma gave one point in the bifurcation diagram, Fig. 5. We applied a symmetric positive disturbance as in Fig. 1(a) in order to obtain the upper half of the bifurcation diagram and a symmetric negative disturbance as in Fig. 1(b) for the lower part of the diagram. We calculated the maximum positive value of the radial component of velocity and plotted it for a positive disturbance on the upper part of the curve, and likewise the most negative value of the radial component of velocity was plotted for a negative disturbance along the lower branch. The critical Marangoni number was obtained by tracing the branch from the lower part of the diagram, since the upper part results in an unstable branch in the vicinity of the bifurcation point. The

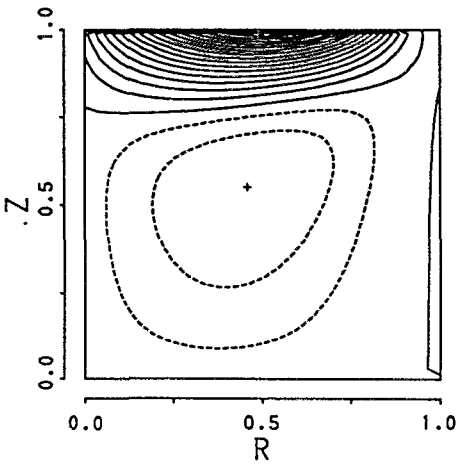

FIG. 6. Isotaches of radial velocity U_r for constant φ, $48\times8\times24$ grid points, $\beta=1.0$, Ma=450, and Fig. 1(a) disturbance. Increment: 0.6434, solid lines: $U_r>0$; dashed lines, $U_r<0$.

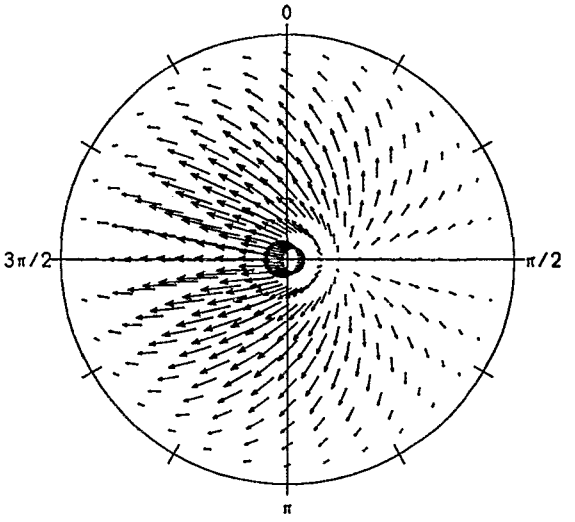

FIG. 7. Vector plot of U_r, U_φ velocities for $z=1.0$, $33\times32\times24$ grid points, $\beta=1.0$, and Ma=390.

unstable region is marked by a dotted line and is drawn by visual interpolation. This could not be obtained by numerical procedure. This is indicative of transcritical bifurcation. The turning point, below which no convection takes place, is obtained by moving along the upper branch with successively lower Marangoni numbers. The Marangoni number was reduced in the following sequence: 450, 430, 414, 410, 405, 400, and 398. The velocities converged to zero for a value of Marangoni number below 398, and so we considered this value to be the point of absolute stability. We also observed that it took a very long time for the energies of the flow to reach a steady value at the point of absolute stability. The number of grid points that we used were 48 for the axial direction, 8 in the azimuthal direction and 24 in the radial direction. We needed at least eight grid points in the azimuthal direction for the Fast Fourier solver used in the numerical code. The increase in the number of axial grid points was appropriate, given the fact that the cell center is skewed toward the interface. This is to be expected, since Marangoni convection is a surface effect, as opposed to Rayleigh convection, which is a domain effect. The obtained flow field is axisymmetric with upflow on the axis for a positive disturbance and downflow for a negative temperature disturbance. Figure 6 shows the radial velocity distribution at a constant azimuthal position. We see that the cell center is indeed skewed toward the interface.

We now discuss the results of our calculation for the case of $\beta=2.0$. To get the bifurcation diagram we used the axisymmetric disturbances in Figs. 1(a) and 1(b). In both cases we started with Ma=1600 and calculated as many time steps as necessary to reach a steady state. To decide whether the convection reached a steady state, we saved the maximum values of each velocity component and the average kinetic energy of each component for every 1000 time steps. We obtained a bifurcation point at Ma=1445 (compare this to the theoretical value of Vrentas *et al.*[10] of 1417.4). Once again we have transcritical bifurcation for the case of axisymmetric disturbances. The grid spacing of $32\times8\times24$ was found to be sufficient to resolve the essential physics.

Finally, we observe that Vrentas *et al.*,[10] as well as Winters *et al.*[12] have noted that the bifurcation diagram becomes more symmetric as we increase the width of the container. We compared the slopes in the branches at the bifurcation point for both our aspect ratios and found them to be 0.071 $U_{r,\max}$/Ma for $\beta=1.0$ and 0.038 $U_{r,\max}$/Ma for $\beta=2.0$. In fact, this is consistent with the derivation of Cloot and Lebon,[11] who showed that two-dimensional disturbances in a *laterally unbounded fluid* give rise to symmetric supercritical bifurcation diagrams.

C. Marangoni convection (nonaxisymmetric disturbances)

We shall give a summary of the results when three-dimensional disturbances are initially imposed on the con-

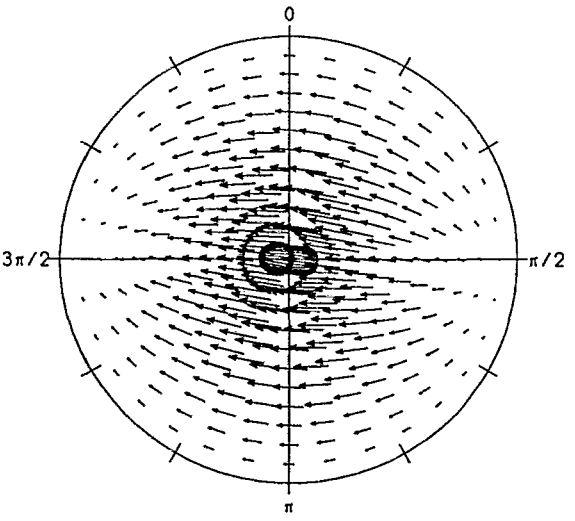

FIG. 8. Vector plot of U_r, U_φ velocities for $z=1.0$, $33\times32\times24$ grid points, $\beta=1.0$, and Ma=340.

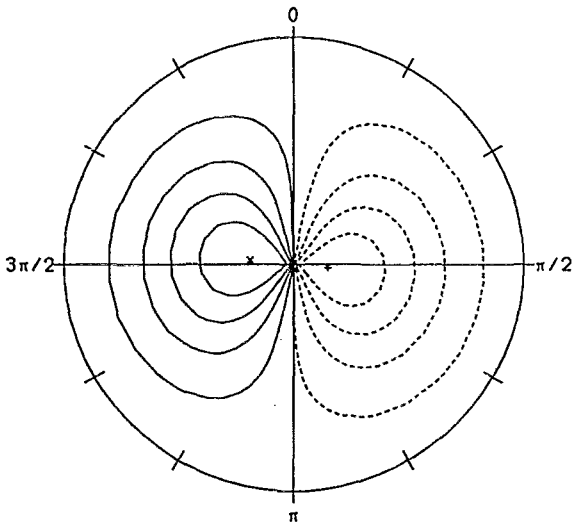

FIG. 9. Isotaches of the radial velocity U_r for $z=1.0$, $33\times32\times24$ grid points, $\beta=1.0$, Ma=340, and a Fig. 1(c) disturbance. Increment: 0.029 95, solid lines: $U_r>0$, dashed lines: $U_r<0$.

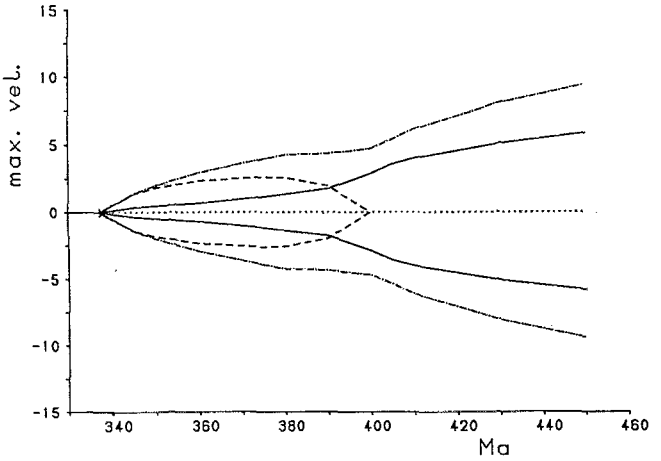

FIG. 11. Bifurcation for $\beta=1.0$ and asymmetric disturbance, maximal velocities plotted against Marangoni number. Solid line: $U_{z,\max}$, dashed line: $U_{\varphi,\max}$, dash–dotted line: $U_{r,\max}$. The bifurcation point is indicated by "x."

ductive state initially. Let us first consider the case of $\beta=1.0$. Here the calculation was done with a grid of $33\times32\times24$, since a comparative study for different grids for $\beta=2.0$ showed this grid to be fine enough to resolve all the major physics. Once again, the negative and positive disturbances corresponding to Figs. 1(c) and 1(d) were imposed. For Ma>400, we obtained a three-dimensional, transient, two roll solution of mode $m=2$. Here the values of the azimuthal velocity converged to zero with time, leading to an axisymmetric steady flow field, similar to the one that we obtained for an axisymmetric disturbance. For Ma=390 we obtained a asymmetric one-cell solution, which looked basically like an $m=1$ cell, but with the center of rotation being shifted to one side of the cylinder. Consequently, the vector plot at $z=1.0$ in Fig. 7 shows a stronger flow in one-half the cylinder. For a nearly critical Marangoni number of Ma=340, the distorted flow field converged to the asymmetric $m=1$ cell that Chen *et al.*[14] report at the bifurcation point, as shown in Fig. 8. If we compare the isotaches of the radial velocity at $z=1.0$ in Fig. 9 for Ma=340 with the ones of Fig. 10 for Ma=390, we note that while the flow profile close to the bifurcation is three dimensional, it has a higher degree of symmetry with upflow in one half and downflow in the other half of the cylinder. Note that the turning point for two-dimensional axisymmetric disturbances was found to be at Ma=398. While the flow field below Ma=398 is three dimensional, it is two dimensional for Ma greater than Ma=398. Thus we have a *second bifurcation* from three- to two-dimensional flow at Ma=398. We depict this in Fig. 11, where we see that the azimuthal component of velocity

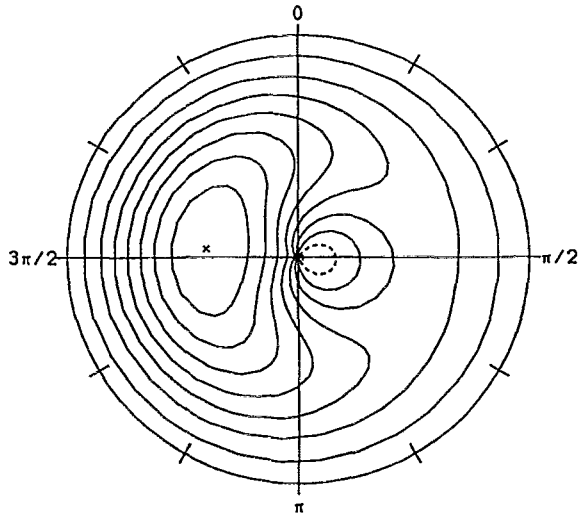

FIG. 10. Isotaches of the radial velocity U_r for $z=1.0$, $33\times32\times24$ grid points, $\beta=1.0$, Ma=390, and a Fig. 1(c) disturbance. Increment: 0.4528, solid lines, $U_r>0$, dashed lines, $U_r<0$.

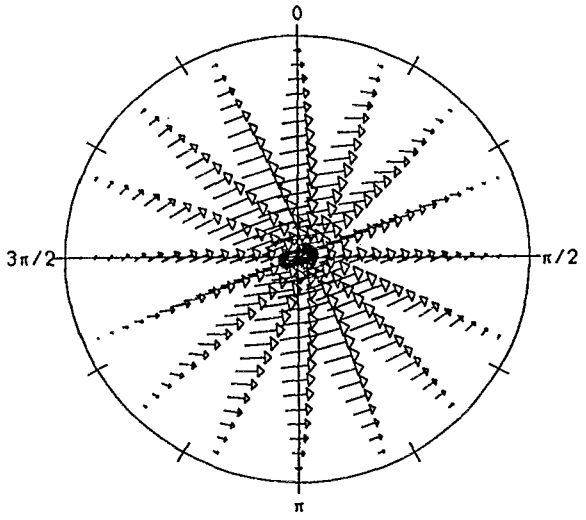

FIG. 12. Vector plot of U_r, U_φ velocities for $z=1.0$, $32\times16\times24$ grid points, $\beta=2.0$, Ma=700, and a Fig. 1(c) disturbance.

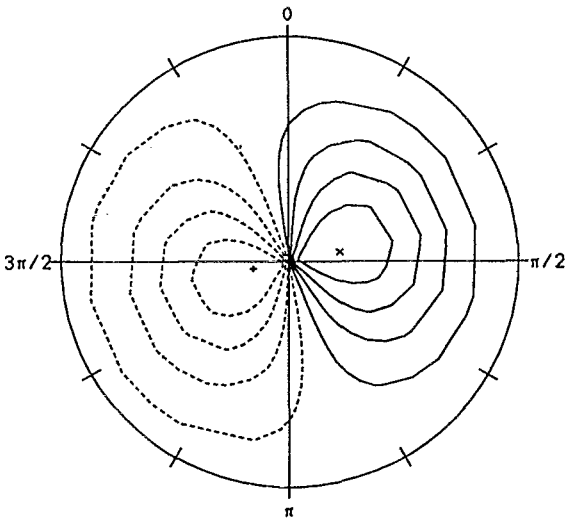

FIG. 13. Isotaches of the radial velocity U_r in a cut plane at $z=1.0$, $32\times16\times24$ grid points, $\beta=2.0$, Ma=340, and a Fig. 1(c) disturbance. Increment: 0.33, solid lines $Ur>0$, dashed lines: $Ur<0$.

vanishes at Ma=398. The bifurcation diagram, Fig. 11, is symmetric and the point of absolute stability, we find is at $Ma_{cr}=339$, which is lower than the Chen *et al.* value of $Ma_{cr}=360$. The bifurcation diagram was obtained by the same procedure as before.

We also studied the case of $\beta=2.0$, where we used a grid of $32\times32\times24$ points. As in the $\beta=1.0$ case, we were able to obtain a bifurcation diagram, which was also symmetric and similar in nature to Fig. 11. Contrary to the case of $\beta=1.0$, there was no transition to an axisymmetric flow field for supercritical Ma numbers. We found the bifurcation point to be at Ma=695. This can only be compared with the extrapolated results of Chen *et al.* In Fig. 12 we present a vector plot, which was taken at the interface for Ma=700. Again we obtained an asymmetric one-cell

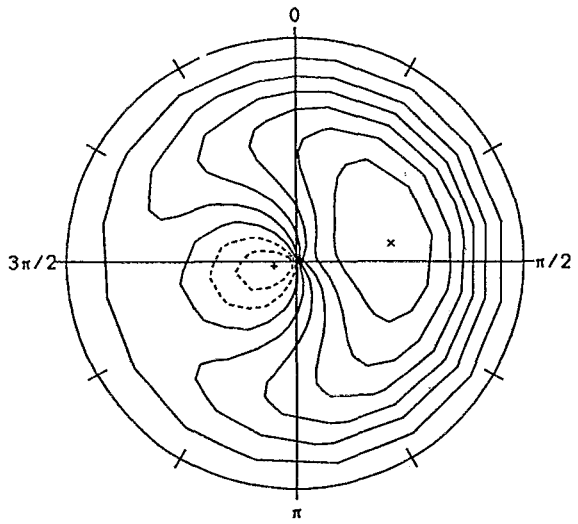

FIG. 14. Isotaches of the radial velocity U_r for $z=1.0$, $32\times16\times24$ grid points, $\beta=2.0$, Ma=3000, and a Fig. 1(c) disturbance. Increment: 4.689, solid lines $U_r>0$, dashed lines: $U_r<0$.

TABLE I. Comparison of critical Ma numbers to others obtained by linearized theory.

Geometry	Vrentas *et al.*,[10] 2-D linearized	Chen *et al.*,[14] 3-D linearized	This work, 3-D numerical
$\beta=1.0$ 2-D	$Ma_{cr}=412$		$Ma_{cr}=414$
$\beta=1.0$ 3-D		$Ma_{cr}=360$	$Ma_{cr}=339$
$\beta=2.0$ 2-D	$Ma_{cr}=1417.4$		$Ma_{cr}=1445$
$\beta=2.0$ 3-D		Extrapolated $Ma_{cr}=650$–700	$Ma_{cr}=695$

flow corresponding to the mode $m=1$. This three-dimensional flow appears more symmetric (see Fig. 13, where the isotaches of the radial velocity are shown), than a flow far from the bifurcation point (see the isotaches for Ma=3000 in Fig. 14). A comparison between our results and those of Rosenblat *et al.*[13] show a similarity in modal structure at the onset of convection for both aspect ratios, i.e., $\beta=1$ and $\beta=2$. These calculated modal patterns imply a unimodal flow across the cylinder diameter with a single node (or a single change in sign) in the azimuthal direction.

Finally, the comparison between the critical Marangoni numbers of Vrentas *et al.*, Chen *et al.*, and this work is presented in Table I. The agreement with the 2-D results of Vrentas *et al.* with a deviation of less than 2% is good, while the comparison to the Chen *et al.* results shows a difference of 6%. This can be explained by the fact that Chen *et al.* presented his results only graphically. Therefore Chen *et al.* values in Table I have to be regarded with some caution.

V. SUMMARY

We have used a numerical code to calculate the flow fields to the complete nonlinear Boussinesq equations. We imposed two- and three-dimensional disturbances, and found that the behavior is a function of grid size. For the pure Rayleigh problem, coarse grids can tell us that a three-dimensional flow structure is possible when actually a finer grid spacing will render a two-dimensional flow field.

For the case of pure Marangoni convection we obtained earlier results that were confirmed by linearized theories for both types of disturbances. Flow profiles that we have calculated show the bifurcation in the supercritical region from three-dimensional to two-dimensional forms. This property was seen to be aspect ratio dependent.

ACKNOWLEDGMENTS

We acknowledge support from the Florida Space Grant Consortium, the A. v. Humboldt Foundation and NASA (Langley) NAG 1-1474.

[1] E. L. Koschmieder, "On convection on a uniformly heated plane," Beitr. Phys. Atmos. **39**, 1 (1966).
[2] K. Stork and U. Müller, "Convection in boxes: An experimental inves-

tigation in vertical cylinders and annuli," J. Fluid Mech. **71**, 231 (1975).
[3]G. A. Ostroumov, *Svobodnaya Convectzia v Ousloviakh Vnoutrennei Zadachi* (State Publishing House, Technico-Theoretical Literature, Moscow, 1952 [English translation, NACA-Tm-1407].
[4]G. Müller, G. Neumann, and W. Weber, "Natural convection in a vertical Bridgman configuration," J. Cryst. Growth **70**, 78 (1984).
[5]G. S. Charlson, and R. L. Sani, "On thermoconvective instability in a bounded cylindrical fluid layer," Int. J. Heat Mass Transfer **14**, 2157 (1971).
[6]G. R. Hardin, R. L. Sani, D. Henry, and B. Roux, "Buoyancy driven instability in a vertical cylinder: Binary fluids with Soret effect. Part I: General theory and stationary stability results," Int. J. Num. Methods Fluids **10**, 79 (1990).
[7]E. Crespo del Arco and P. Bontoux, "Numerical solution and analysis of asymmetric convection in a vertical cylinder: An effect of Prandtl number," Phys. Fluids A **1**, 1348 (1989).
[8]G. Neumann, "Three dimensional numerical simulation of buoyancy driven flows in vertical cylinders heated from below," J. Fluid Mech. **214**, 559 (1990).
[9]G. Neumann, "Berechnungen der thermische auftriebskonvection in modellsystem zur kristallzuechtung," Dissertationsschrift, Erlangen, 1986.
[10]J. S. Vrentas, R. Narayanan, and S. S. Agrawal, "Free surface convection in bounded cylindrical geometry," Int. J. Heat Mass Transfer **24**, 1513 (1981).
[11]A. Cloot and G. Lebon, "A nonlinear stability analysis of the Bénard–Marangoni problem," J. Fluid Mech. **145**, 447 (1984).
[12]K. H. Winters, Th. Plesser, and K. A. Cliffe, "The onset of convection in a finite container due to surface tension and buoyancy," Physica D **29**, 387 (1988).
[13]S. Rosenblat, S. H. Davis, and G. H. Homsy, "Nonlinear Marangoni convection in bounded layers Part 1—Circular cylindrical containers," J. Fluid. Mech. **120**, 91 (1982).
[14]J-C. Chen, J-Y. Chen, and Z.-C. Hong, "Linear Marangoni instability of a fluid in circular cylindrical containers," Paper No. IAF-91-393, 42nd Congress of the International Astronautical Federation, Montreal, October 1991.
[15]A. J. Chorin, "Numerical solution of the Navier–Stokes equations," Math. Comput. **22**, 745 (1968).
[16]L. Schmitt, "Numerische simulation turbulenter grenzschichten (large eddy simulation)," Insitutsbericht Nr. 82/2, Lehrstuhl für Strömungsmechanik, T. U. München, 1982.
[17]P. Stroebel, "Untersuchungen von temeraturverteilungen in modellfuessigkeiten bei vertikalen bridgmananordnungen," diplomarbeit, Universitaet Erlangen—Nuernberg, Institut fuer Werkstoffwissenschaften, 1984, Vol. 4.